A&A 487, 951–963 (2008)
DOI: 10.1051/0004-6361:20079240

Astronomy & Astrophysics

Global properties of the H I distribution in the outer Milky Way

Planar and extra-planar gas

P. M. W. Kalberla and L. Dedes

Argelander-Institut für Astronomie, Universität Bonn, Auf dem Hügel 71, 53121 Bonn, Germany
e-mail: `[pkalberla;ldedes]@astro.uni-bonn.de`

Received 13 December 2007 / Accepted 31 March 2008

ABSTRACT

Context. The determination of the global structure of the planar and extra-planar Milky Way H I disk depends critically on a reliable database but also on reasonable assumptions about the shape of the Milky Way rotation curve.
Aims. We derive the 3D H I volume density distribution for the Galactic disk out to $R \sim 60$ kpc.
Methods. Our analysis is based on parameters for the warp and rotation curve derived previously. The data are taken from the Leiden/Argentine/Bonn all sky 21 cm line survey.
Results. The Milky Way H I disk is significantly warped but shows a coherent structure out to $R \sim 35$ kpc. The radial surface density distribution, the densities in the middle of the warped plane, and the H I scale heights all follow exponential relations. The radial scale length for the surface density distribution of the H I disk is 3.75 kpc. Gas at the outskirts for $40 \lesssim R \lesssim 60$ kpc is described best by a distribution with an exponential radial scale length of 7.5 kpc and a velocity dispersion of 74 km s^{-1}. Such a highly turbulent medium fits also well with the average shape of the high velocity profile wings observed at high latitudes. The turbulent pressure gradient of such extra-planar gas is on average in balance with the gravitational forces. About 10% of the Milky Way H I gas is in this state. The large scale H I distribution is lopsided; for $R \gtrsim 15$ kpc there is more gas in the south. The H I flaring indicates that this asymmetry is caused by a dark matter wake, located at $R \sim 25$ kpc in direction of the Magellanic System.
Conclusions. The H I disk is made up of two major components. Most prominent is the normal H I disk which can be traced to $R \sim 35$ kpc. This is surrounded by a patchy distribution of highly turbulent gas reaching large scale heights but also large radial distances. At the position of the Sun the exponential scale height in the z direction is 3.9 kpc. This component resembles the anomalous gas discovered previously in some galaxies.

Key words. Galaxy: disk – Galaxy: halo – Galaxy: structure – Galaxy: kinematics and dynamics – ISM: structure

1. Introduction

The gaseous content of galaxies is a crucial counterpart to the stellar population but has the additional advantage that it can be traced far beyond the stellar population, radially but also perpendicular to the disk. Stars are born out of gas condensations and their deaths affect the three-dimensional evolution of the Galactic disc. The gas traces such activities. Here we are interested in the steady state situation caused by dynamical processes as described e.g. by de Avillez (2000). The 21 cm line traces these processes, in particular the diffuse part of the interstellar medium (ISM). A thin disk is expected in the plane, overlaid by a thick H I disk which is associated with an ionized layer. Depending on the supernova rate in the underlying disc a more or less established disc-halo interface is expected.

Most prominent, comparing the gaseous content of galaxies with the stellar distribution, is the large radial extent of the gaseous disk. The outer part is only slightly affected by the stellar disk but traces environmental influences such as influences from the intergalactic medium. We explore global parameters for layers above the disk and gas at the outskirts of the Milky Way. For such an analysis we need to determine the properties of the dominant part of the H I distribution first, i.e. the H I disk which co-rotates with the stellar disk. Knowing the properties of the gas within the disk we may proceed to determine the nature of the gas around this disk.

In Sect. 2 we briefly introduce the database and the conversion of brightness temperatures $T_{\mathrm{B}}(l, b, v)$ to densities $n(R, z, \phi)$. The observer's location inside the Galactic disk causes some ambiguities and constraints that need to be discussed. In Sect. 3 we derive radial dependencies of the average surface density distribution within the disk. This is followed in Sect. 4 by a discussion of average properties of the mid-plane volume densities. We find that the gas distribution within the Milky Way H I disk is approximately exponential for a large part of the disk. The gas properties at $R \gtrsim 35$ kpc differ significantly; this is studied in Sect. 5. At the outskirts we find that the H I distribution needs to be described as a highly turbulent phase. In Sect. 6 we consider the H I distribution at the polar caps. We require hydrostatic equilibrium and derive a velocity dispersion of $\sigma = 74$ km s^{-1} for the halo gas phase. Such a phase explains not only the H I distribution at the outskirts but also the average local emission high above the disk. About 10% of the H I is in this phase and we demonstrate that the Milky Way would look very similar to NGC 891 or NGC 2403 if it were observed edge-on at large distances. Section 7 contains a summary.

2. Database and derived density distribution

Our analysis is based on the Leiden/Argentine/Bonn (LAB) H I line survey (Kalberla et al. 2005). This survey combines the southern sky survey of the Instituto Argentino de Radioastronomía (IAR) (Bajaja et al. 2005) with an improved version of the Leiden/Dwingeloo Survey (LDS) (Hartman & Burton 1997). Currently, this is the most sensitive Milky Way H I line survey with the most extensive coverage both spatially and kinematically. The line profiles have been corrected for spurious sidelobe emission; we expect therefore that profile wings, most critical for our investigations, are only mildly contaminated by instrumental problems.

2.1. The density distribution $n(R, z, \phi)$

All the individual steps necessary to convert the observed brightness temperature distribution $T_{\rm B}(l, b, v)$ as a function of galactic longitude, latitude and LSR velocity to densities $n(R, z, \phi)$ have been described by Kalberla et al. (2007). We use cylindrical coordinates R, z, ϕ to describe the Milky Way disk; $\phi = 0$ is in direction $l = 0$. We use the IAU recommendations for the galactic constants; $R_\odot = 8.5$ kpc and $v_\odot = 220$ km s^{-1}.

Figure 1 shows several global properties of the Galactic H I density distribution. We have chosen a common logarithmic transfer function to cover the high dynamic range of the density fluctuations within the Galactic disk. The average extension of the flaring disk layer is indicated. The thin white lines indicate the thickness of the disk at a 3σ level of the second moment fitted by Kalberla et al. (2007). The warp is obvious for $R \gtrsim 15$ kpc as a sine-wave pattern. With increasing distance, the southern part of the disk, $-180° \lesssim \phi \lesssim 0°$, returns to $z \sim 0°$ while the northern part, $0° \lesssim \phi \lesssim 180°$, bends up strongly and becomes increasingly disrupted. Within the galactic plane several shells are detectable; some of them have very low central densities. All kind of spurs, arcs, filaments, and chimneys are visible, indicating violent interactions for most parts of the disk, most pronounced for $R \lesssim 20$ kpc.

We do not discuss details visible in Fig. 1 but a few comments concerning the $T_{\rm B}(l, b, v)$ to $n(R, z, \phi)$ conversion are necessary. The shape of the Milky Way rotation curve, but also the location of the Sun within the Galactic plane, causes complex geometrical transformations. A white line is plotted in Fig. 1 at latitudes $|b| = 30° \pm 0.5°$ for visualization. Some ambiguities are discussed next.

Local gas at low velocities may cause spurious features in the density distribution, most serious for $|v_{\rm LSR}| < 10$ km s^{-1}. These regions have been disregarded, indicated by the black color in Fig. 1. Figure 2 displays the velocity field at mid-plane. The central green region, enclosed by isophotes, corresponds to $|v_{\rm LSR}| < 10$ km s^{-1}. There are some more regions with unreliable kinematic distances. In the direction of the Galactic center, we discarded data originating from $|R| < 3.5$ kpc. This region, approximately the extent of the bar, is affected by ambiguities due to large velocity dispersions of the emission lines (Weiner & Sellwood 1999, Fig. 8). Low dv/dR values, predominantly at $|\phi| \lesssim 30°$, $\phi \gtrsim 150°$, and $\phi \lesssim -150°$ introduce additional distance uncertainties. We strictly exclude these regions from further analysis and use for the northern part of the Galactic plane the range $30° < \phi < 150°$ and $210° < \phi < 330°$ for the southern part.

A fraction of the observed H I gas distribution is presumably not associated with the disk. Intermediate and high velocity clouds (IVCs and HVCs, respectively) are most probably located above the disk (van Woerden et al. 2004). One might think that such features should be excluded from the database prior to the determination of $n(R, z, \phi)$ for the H I disk. We emphasize that no such filtering was applied to the observations.

The scale height of the H I disk and the mid-plane density was determined by adaptive filtering of the volume density distribution. The basic underlying assumption is that the disk can be characterized as a homogeneous gas layer in circular rotations, for details we refer to Kalberla et al. (2007). The thin white lines in Fig. 1 characterize the extension of the gas in the Galactic plane. We display the 3σ level of the second moment fitted by Kalberla (2007) to the flaring gas layer. The 3σ limit is somewhat arbitrary, a different measure might be chosen to distinguish between disk and extra-planar gas. Whatever criteria might be applied, Fig. 1 shows that most of the H I gas settles down in a thin disk phase while there remains an extra-planar contribution, either diffuse or filamentary, but in most cases unambiguously associated with the disk. This extra-planar part was excluded when calculating disk scale heights and the mid-plane densities, but was left in the database for the rest of the analysis. There is direct evidence that on average 5% of the H I gas is located outside the disk (Fig. 12). As discussed later, this is a lower limit only.

Inside the solar circle the translation between distance and velocity is ambiguous because there are two positions along the line of sight that have the same velocity. These positions, however, may have different z distances, so their densities may differ accordingly. We modeled the expected flaring of the H I distribution and weighted the derived quantities correspondingly. Our method is comparable to that of Nakanishi & Sofue (2003), except that they use a sech^2 approach (Spitzer 1942) in place of our more detailed model. Our model matches well with the observed flaring; for a verification of the model we refer to Kalberla et al. (2007, Fig. 14).

For a description of the global properties of the Galactic H I disk we discuss in the next sections the first three moments of the $n(R, z, \phi)$ distribution; the surface density, $\Sigma(R, \phi)$, the first moment $z_0(R, \phi)$, representing the mid-plane, and the second moment $\sigma(R, \phi)$, representing the scale height of the gas. In addition we derived characteristic mid-plane volume densities $n_0(R, \phi)$ for positions $z_0(R, \phi)$, averaging over $z_0(R, \phi) \pm 0.6\, \sigma(R, \phi)$.

3. The average radial surface density distribution

Figure 3 displays average surface densities determined for the total disk, but also for azimuth $30° < \phi < 150°$ (north) and $210° < \phi < 360°$ (south) separately. There are some deviations between north and south, we therefore derived the detailed surface density distribution across the disk in individual sectors of $\Delta\phi = 20°$. Figure 4 displays the results separately for both parts of the disk. Strong fluctuations, typically within a factor of two, with a correlation length of a few kpc are common. Some of the modulations are caused by a spiral structure (Levine et al. 2006a,b; Kalberla et al. 2007).

Figure 4 confirms the general systematic differences between north and south. Most striking, however, are two regions with exceptional low fluctuations; in the north for $15 \lesssim R \lesssim 20$ kpc and in the south for $25 \lesssim R \lesssim 30$ kpc. A comparison with the mass model and the flaring data from Kalberla et al. (2007, Figs. 18 and 19) indicates that these regions are located at the outer edge of the dark matter ring structures that were needed to explain the observed gaseous flaring. These structures have different locations in the northern ($R \sim 13$ kpc) and southern part ($R \sim 18.5$ kpc) of the Galactic disk but extend in azimuth over at least 120°.

Despite all the scatter, the global radial surface density distribution appears to follow an exponential law over a broad

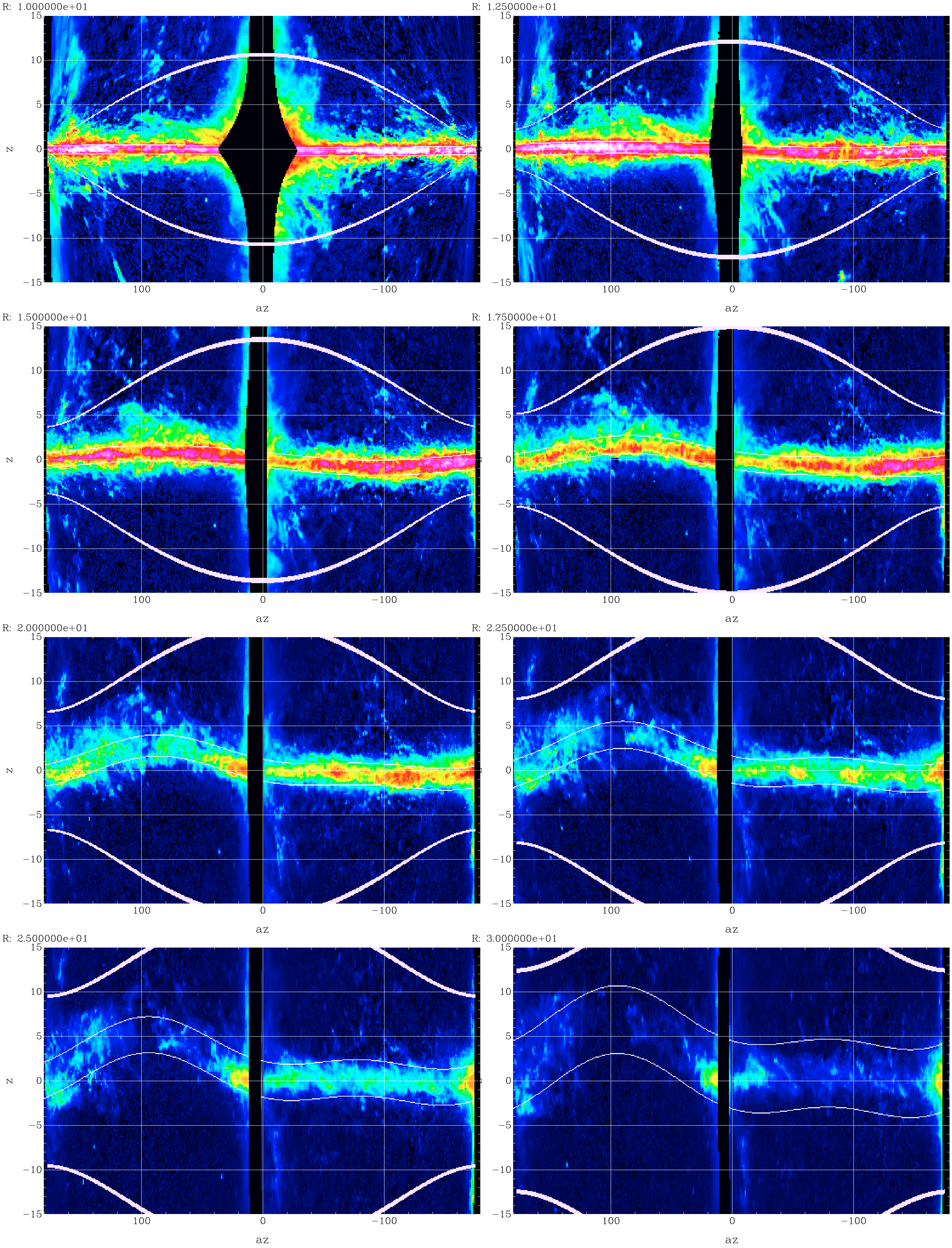

Fig. 1. Derived volume density distribution at R = 10, 12.5, 15, 17.5, 20, 22.5, 25, 30 kpc (*top to bottom*). Locations affected by local emission with $|v_{\mathrm{lsr}}| < 10\ \mathrm{km\,s^{-1}}$ are flagged dark. We display densities $n < 0.5\ \mathrm{cm^{-3}}$. A logarithmic transfer function was chosen to emphasize low densities. The thin white lines indicate the average flaring at a 3σ level and enclose the warped disk. The thick white lines indicate latitudes $|b| = 30° \pm 0.5°$.

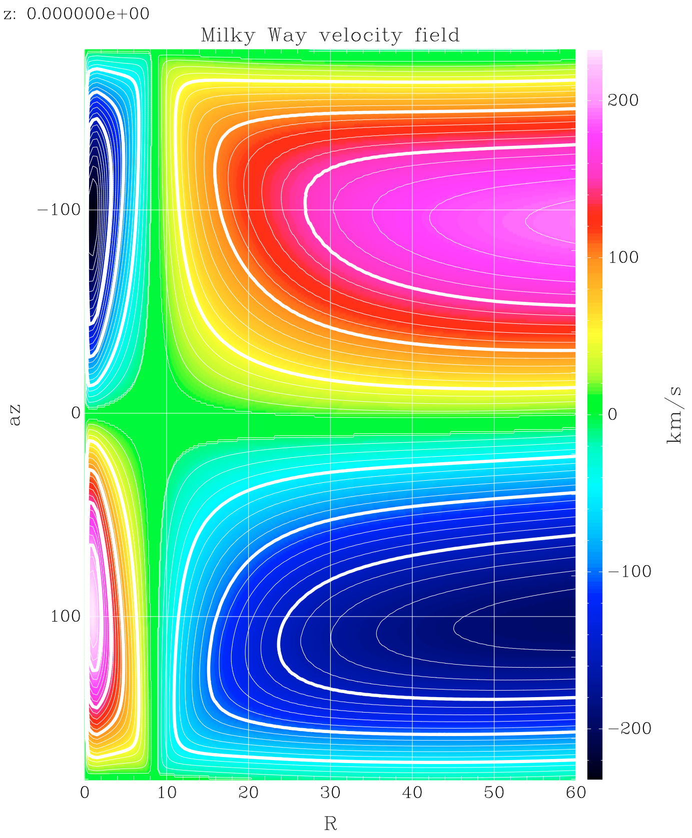

Fig. 2. Milky Way velocity field at mid-plane for the mass distribution derived by Kalberla et al. (2007). The isophotes indicate velocities $-190 < v_{\rm lsr} < 190$ km s^{-1} in steps of 10 km s^{-1}. The thick lines are at $|v_{\rm lsr}| = 50$, 100 and 150 km s^{-1}.

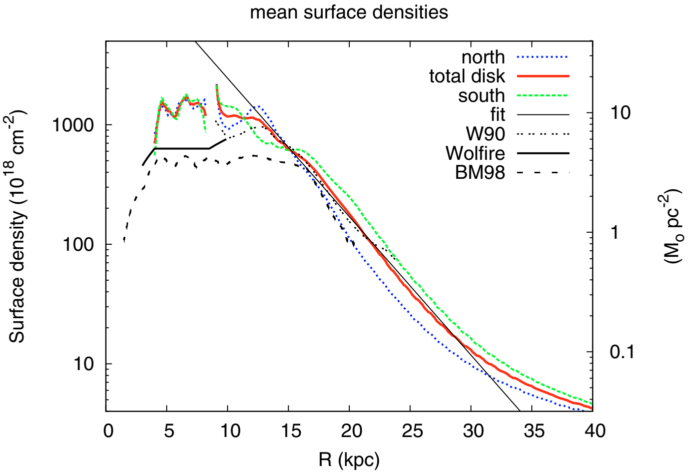

Fig. 3. Derived mean surface densities of the H I gas perpendicular to the disk (red). The dotted blue line gives $N_{\rm H}(R)$ in the northern, the dotted green line in the southern part of the Milky Way. The dashed black line reproduces the distribution published by Binney & Merrifield (1998, BM98) in Fig. 9.19. Wolfire et al. (2003) (thick black line) used partial data from Wouterloot et al. (1990, W90).

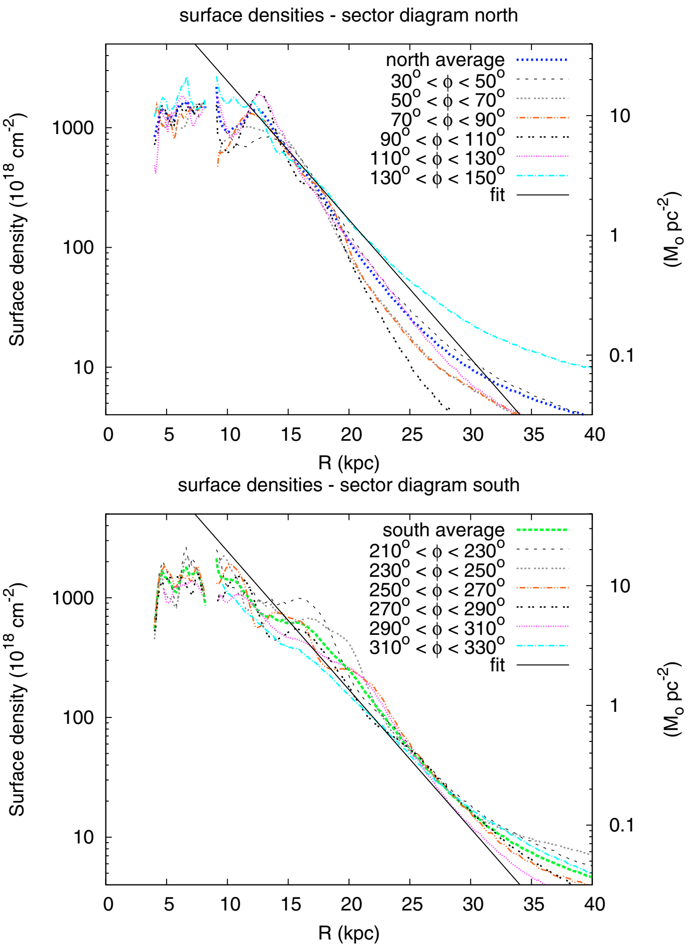

Fig. 4. Systematic variations of the average H I surface density distribution determined in 20° wide sectors for $30° < \phi < 150°$ (north) and $210° < \phi < 330°$ (south). For comparison with Fig. 3 the fit (black) and total averages for north and south (blue and green respectively) are given.

radial range. We approximate the mean surface density distribution by $\Sigma(R) \sim s_0 \cdot {\rm e}^{-(R-R_\odot)/R_{\rm s}}$ with $s_0 = 30\ M_\odot$ pc^{-2} and $R_{\rm s} = 3.75$ kpc. The exponential disk approximation is reasonable for $12.5 \lesssim R \lesssim 30$ kpc. For $R \lesssim 12.5$ kpc the surface densities saturate at approximately $\Sigma_{\rm inner} \sim 10\ M_\odot$ pc^{-2}. This result is in clear conflict with the contemporary knowledge from reviews (Dickey & Lockman 1990), and text books; we reproduce in Fig. 3 the distribution of Binney & Merrifield (1998, Fig. 9.19). Dickey and Lockman give $\Sigma = 5\ M_\odot$ pc^{-2}, the average surface densities for $R \lesssim 18$ kpc according to Binney & Merrifield (1998) is even less. For $R \gtrsim 18$ kpc our data agree with Binney & Merrifield (1998, Fig. 9.19), a general scale error cannot explain the problem.

Discrepancies in Fig. 3 need a detailed discussion, fortunately this is simplified greatly by a recent review (Lockman 2002a, Sect. 4.3). Figure 9.19 of Benny & Merrifield (1998) dates back to Dame (1993) who used data provided by Lockman (1988). Lockman studied two cases, a surface density distribution for a flat rotation curve and alternatively the case of a curve that is flat for $R < R_\odot$, rising at a rate ${\rm d}v/{\rm d}R = 2$ km s^{-1} kpc $^{-1}$ up to $2\ R_\odot$ and staying flat afterwards. In both cases it was assumed that the scale-height of the H I layer is constant. Some unspecified data were "arbitrary scaled by a factor of 2" by Dame to match other results. The case of a rising rotation curve was then adopted by Binney & Merrifield (1998, Fig. 9.19) as characteristic for the Milky Way.

A slightly different surface density distribution, also plotted in Fig. 3, was used by Wolfire et al. (2003), we refer to their detailed discussion. These authors match $\Sigma = 5\ M_\odot$ pc^{-2} according to Dickey & Lockman (1990) with surface densities derived by Wouterloot et al. (1990). Their curve rises for

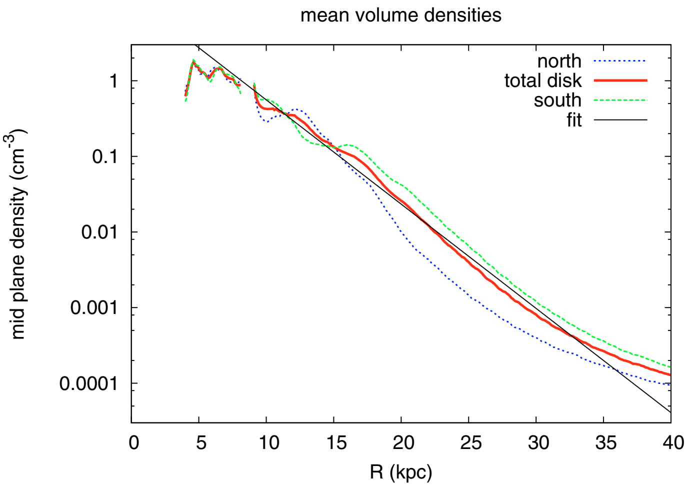

Fig. 5. Derived average mid-plane volume density of the H I gas (red). The dotted blue line gives $n(R)$ in the north ($30^\circ < \phi < 150^\circ$), the dotted green line in the southern part of the Milky Way ($210^\circ < \phi < 330^\circ$). The black line represents an exponential fit with a radial scale length of 3.15 kpc.

$R \gtrsim 10$ kpc. At $R \sim 12.5$ kpc it matches our average surface density distribution and at larger distances our results agree well with Wouterloot et al. (1990), their data are also plotted in Fig. 3. In general we have for $R \gtrsim 10$ kpc a good agreement with Henderson et al. (1982); Kulkarni et al. (1982); Diplas & Savage (1991); Voskes (1999); Levine et al. (2006a,b).

Attempting to explain the discrepancies for $R \lesssim 10$ kpc, the determination of H I surface densities close to $R_{\odot}$ may be subject to serious uncertainties, this was discussed in Sect. 2. In addition we found large biases caused by the assumption that the H I gas at $|z| > 0$ kpc is strictly co-rotating with gas at the mid-plane (Kalberla et al. 2007, see Figs. 3 and 5 for the flaring). Such biases may depend on the methods used. For a co-rotation we derive a 10% lower surface density for $R \lesssim 12.5$ kpc, at the same time the exponential scale length increases from $R_{\mathrm{s}} = 3.75$ kpc to $R_{\mathrm{s}} = 4$ kpc. The slope is consistent with previous results (Henderson et al. 1982; Diplas & Savage 1991; Voskes 1999; Levine et al. 2006a,b) but the average surface density for $R \lesssim 12.5$ kpc is still discrepant. We tested the case of a rising rotation curve as proposed by de Boer et al. (2005) with a peak rotational velocity of 250 km s^{-1} but found no significant changes of the local surface density. This most probably is caused by the fact that locally this rotation curve is flat. We question whether a rotation curve with a local rate $\mathrm{d}v/\mathrm{d}R = 2$ km s^{-1} kpc $^{-1}$ is realistic for the Milky Way.

4. Average radial mid-plane volume densities

Figure 5 displays the average mid-plane volume density distribution $n(R, z_0)$ for the total disk, for $30^\circ < \phi < 150^\circ$ (north), and $210^\circ < \phi < 330^\circ$ (south). Figure 6 shows how the volume densities depend on azimuth; these plots reproduce for $R \gtrsim 12.5$ kpc the same trends as seen before in the surface densities (Fig. 4).

For $7 \lesssim R \lesssim 35$ kpc the average mid-plane volume density follows approximately an exponential distribution, $n(R, z_0) \sim n_0 \cdot \mathrm{e}^{-(R-R_{\odot})/R_{\mathrm{n}}}$ with $n_0 = 0.9$ cm^{-3} and $R_n = 3.15$ kpc. This line is drawn in Figs. 5 and 6.

The surface density is essentially a product of mid-plane volume density and the corresponding flaring. The fact that surface density as well as mid-plane volume density can be approximated by an exponential function implies that the flaring also needs to be described well by an exponential function. We confirm this as the fit $h_R = h_0\, \mathrm{e}^{(R-R_{\odot})/R_0}$ kpc with $h_0 = 0.15$ kpc and $R_0 = 9.8$ kpc for the half width at half maximum provides a good approximation to the observed flaring (Kalberla 2007, Fig. 6) for $5 \lesssim R \lesssim 35$ kpc. For $R \gtrsim 35$ kpc, data and fit diverge rapidly. Figure 7 re-plots for comparison the flaring derived in Kalberla et al. (2007).

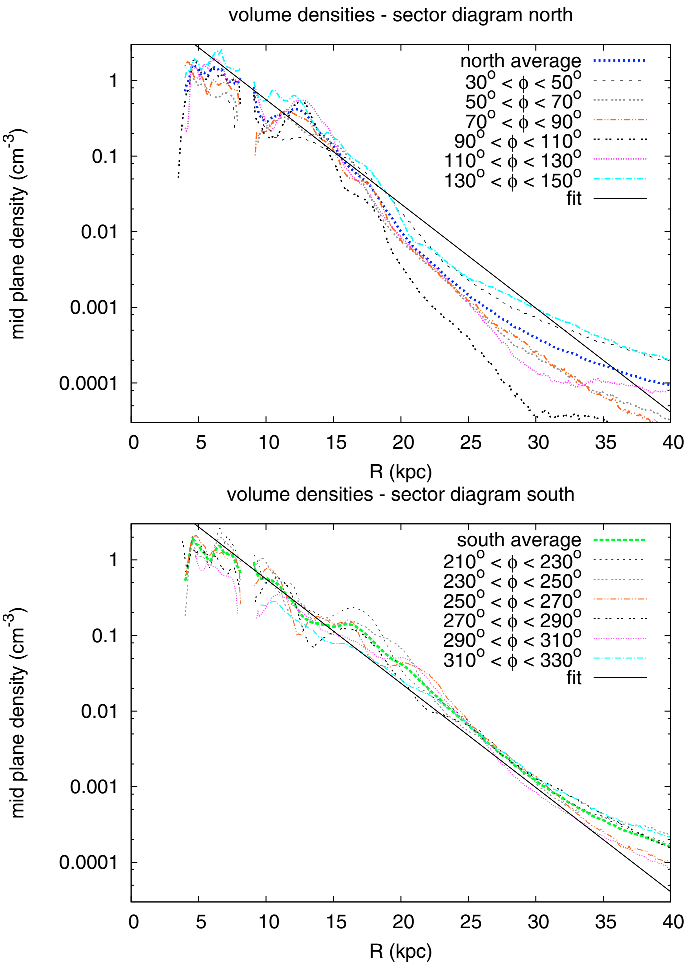

Fig. 6. Systematic variations of the average H I volume density distribution determined in 20° wide sectors for $30^\circ < \phi < 150^\circ$ (north) and $210^\circ < \phi < 330^\circ$ (south). For comparison with Fig. 5 the fit (black) and total averages for north and south (blue and green respectively) are given.

The finding that surface density, mid-plane density, and flaring can be represented by exponential functions does not reflect a general property of galactic disks but is closely related to the rotation curve used, hence it depends on the Galactic mass distribution. In particular, the divergence of the exponential fit from the observed flaring for $R \gtrsim 35$ kpc is caused by the shape of the gravitational potential which is oblate for small radii but changes to prolate in the outer part. The transition region, the location where we have a potential similar to the spherical case, is at $R \sim 35$ kpc (for a more detailed discussion see Kalberla 2003, Sects. 5.2.2 and 5.2.3). This radius defines the "edge" of the disk.

5. The Galactic outskirts

Common to the average surface density and the average mid-plane density is that they both do not indicate a boundary of the

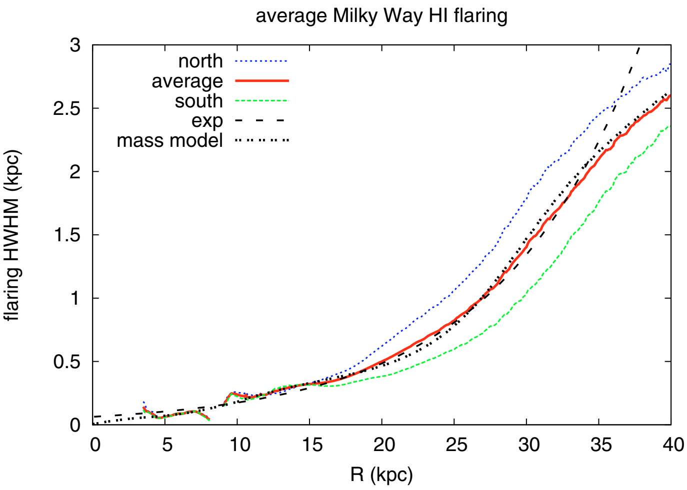

Fig. 7. Derived mean flaring of the H I gas (red). The dotted blue line holds for the northern, the dotted green line for the southern part of the Milky Way. For comparison an exponential fit for $R < 35$ kpc is plotted (long dashed), also the flaring according to the model by Kalberla et al. (2007).

Milky Way disk with a truncation of the observable H I distribution. Beyond a radius of ~35 kpc the gas appears to have a more shallow distribution. We study this behavior in more detail.

5.1. The warp, scalloping

The Galactic warp was shown by Kalberla et al. (2007, Figs. 16 and 17) to be well defined for $R \lesssim 40$ kpc. Three basic modes exist with slowly variable phases. The outermost part of the warp for $R \gtrsim 30$ kpc contains higher Fourier modes, thus the disk is scalloping. We determine these modes by subtracting the basic warp modes 0 to 2 from the derived mid-plane positions. For the residuals we use a least square fitting algorithm to search for oscillations with higher frequencies. We determine simultaneously amplitude, frequency, and phase. For various initial estimates in frequencies, corresponding to modes 3 to 20, we demand that the fit stays stable in frequency. As a result, we find oscillations with scalloping modes 10 to 20. The significance of these higher warp modes is low for $R \lesssim 30$ kpc. The associated power, defined by the squares of the amplitudes, is below 0.6% of the total warp power in this range. For $R \gtrsim 30$ kpc we find a significant contribution; the preferred modes are 10 and 13. The relative strength of the scalloping increases linearly up to ~2.5% of the total warp power at $R = 40$ kpc. This is shown in Fig. 11 (magenta). The warp can be traced further with the scalloping power increasing to larger distances but the significance of the warp is highly questionable there.

Our analysis is complementary to Levine et al. (2006a) who used Morlet wavelet transforms for an analysis of the warp out to $R = 30$ kpc. They concluded that the $m = 10$ and 15 scalloping modes are well above the noise, but localized; this suggests that the scalloping in this range does not pervade the whole disk, but only local regions. We applied a straightforward sine wave analysis which is insensitive to local oscillations and found some coherent grouping of higher mode oscillations, spreading out over several annuli, although insignificant for fits at individual radii. Only for $R \gtrsim 30$ kpc does scalloping become powerful enough to be significant in each case. This result supports Saha & Jog (2006) who concluded that scalloping at high modes has to be restricted to the outermost part of a galaxy.

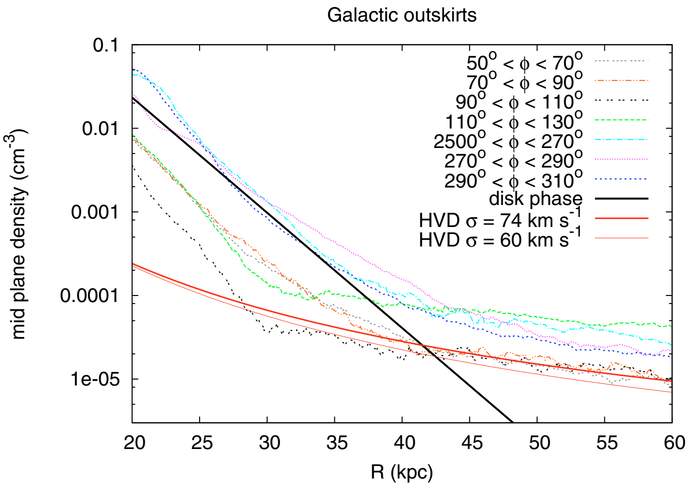

Fig. 8. Average mid-plane volume densities for 20° wide radial sectors in the Milky Way. For comparison the fitted distribution of the HVD gas is given (red solid lines).

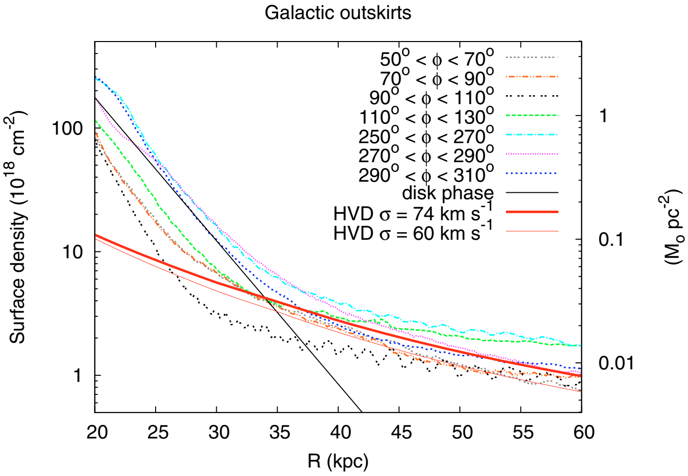

Fig. 9. Average mid-plane surface densities for 20° wide radial sectors in the Milky Way. For comparison the fitted distribution of the HVD gas is given (red solid lines).

5.2. Mid-plane and surface densities

Figure 8 plots average mid-plane volume densities for 20° wide sectors as used before. Comparing the distributions with the exponential fit from Fig. 5 we find a shallower decrease for $R \gtrsim 35$ kpc. Average surface densities displayed in Fig. 9 show the same trend. Both plots suggest that the H I gas in the outskirts differs significantly from the H I gas in the Galactic disk, which was fitted before by an exponential law.

Tracing the shallow H I volume density distribution at large distances back to the observed brightness temperature distribution we find that these belong to weak emission profile wings. The wings cannot be explained by emission from the cold or the warm neutral medium (CNM and WNM, respectively). Similar wings have been found in the Leiden/Dwingeloo Survey (Hartmann & Burton 1997) at high latitudes and Kalberla et al. (1998, Fig. 1) argued that the wings can be traced to low latitudes; this implies large distances. The LDS profile wings could be fitted well by a pervasive emission component with a high velocity dispersion (HVD) of ~60 km s^{-1}.

It is tempting to associate the shallow density distribution, visible in Figs. 8 and 9, with such an HVD component.

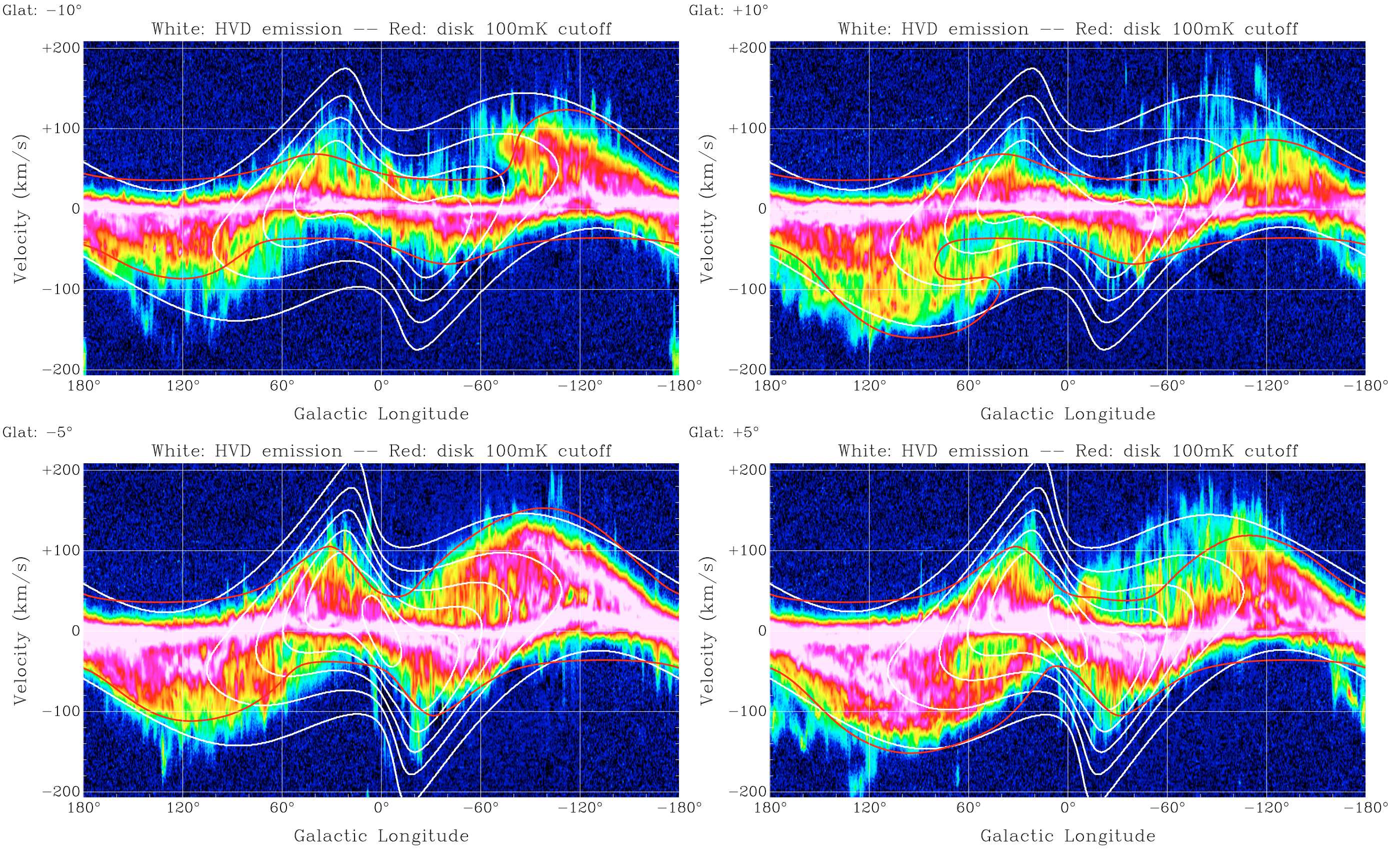

Fig. 10. Position-velocity diagrams for the Milky Way H I brightness termerature at latitudes –10°, –5° (*left*) and 10°, 5° (*right*). The white isophotes display HVD emission from the model (10% to 90% in steps of 10%), the red isophote marks an average disk emission of 100 mK. A logarithmic transfer function was used for $T_{\rm B} < 30$ K.

The proof, however, is not straightforward. The observed profile wings must originate from a diffuse distribution of unresolved H I clumps and it is a priori not obvious how these wings translate into the corresponding volume density distribution. We therefore modeled the H I emission for an HVD component with a radial scale length of $R_{\rm HVD} = 7.5$ kpc (Kalberla 2003). Synthetic emission lines were calculated for a dispersion of $\sigma_{\rm HVD} = 60$ km s^{-1} and $\sigma_{\rm HVD} = 74$ km s^{-1} (differences will be discussed in Sect. 6.1). Next we derived the surface density and volume density distribution for the synthetic HVD distribution by applying the same procedures as used before for the analysis of the LAB observations. Figures 8 and 9 show the result. The HVD component is weak in comparison to the disk emission at low radii but dominates the H I distribution at the outskirts for $R \gtrsim 35$ kpc.

The assumption of a pervasive extended HVD H I component agrees well with the data (Figs. 8 and 9). The HVD model with $\sigma_{\rm HVD} = 74$ km s^{-1} fits slightly better. As discussed before for the disk gas, there are systematic differences between north and south. Where is the HVD emission located in the observed $T_{\rm B}(l, b, v)$ distribution?

In the Galactic outskirts the HVD gas becomes noticeable for $R \gtrsim 35$ kpc and the range $50° \lesssim \phi \lesssim 130°$ and $250° \lesssim \phi \lesssim 310°$ is useful for its analysis. The translation between $T_{\rm B}(l, b, v)$ and $n(R, z, \phi)$, discussed in Sect. 2, is such that this gas must appear at high negative velocities for longitudes $40° \lesssim l \lesssim 140°$ and at high positive velocities for $310° \gtrsim l \gtrsim 220°$. Figure 10 gives a few examples for the observed H I brightness temperature distribution, l–v slices at latitudes $b = -10°, -5°, 5°$, and $b = 10°$.

Extra-planar H I gas has a low volume filling factor. Correspondingly, a patchy low level emission is expected in the region of interest. A second property is the high velocity dispersion for this clumpy medium. This shows up as extensions (stripes) in the v direction. Figure 10 shows a rather complicated pattern. A part of the emission may originate from large distances but the warp makes it difficult to determine whether individual filaments belong to the disk (having a low velocity dispersion) or not. For a clearer picture we calculated the expected average disk emission and plotted the positions where this emission should reach a level of 100 mK (red isophotes). Then we include the average emission according to the HVD model in Fig. 9 (white isophotes).

In the inner Galaxy the HVD emission is clear in Fig. 10 with high velocities against the disk emission at longitudes $l \sim 25°$ and $l \sim 335°$. The region at $l \sim 335°$ is currently studied by Alyson Ford with the Parkes telescope. The region $l \sim 25°$ was investigated in detail by Lockman (2002b, 2004). Numerous small clumps can be traced with the GBT up to distances of several hundred pc above the mid-plane. These clumps are usually unresolved in the LAB survey but contribute to the observed surface densities.

Comparing the HVD model emission with observations, we find for some regions significant deviations from the expected distribution. This reflects the fact that HVCs and IVCs are grouped in complexes, while there are also regions with little extra-planar H I gas.

5.3. Asymmetric gas distribution

Figures 3 to 9 show a pronounced asymmetry of the gas distribution for $R \gtrsim 20$ kpc. For a more quantitative comparison

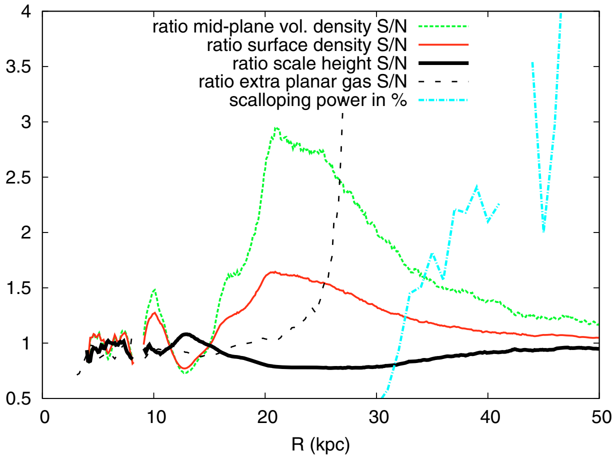

Fig. 11. Asymmetry of mid-plane volume densities, surface densities, and scale heights characterized by their south/north ratios S/N. In addition the warp scalloping power in % is given.

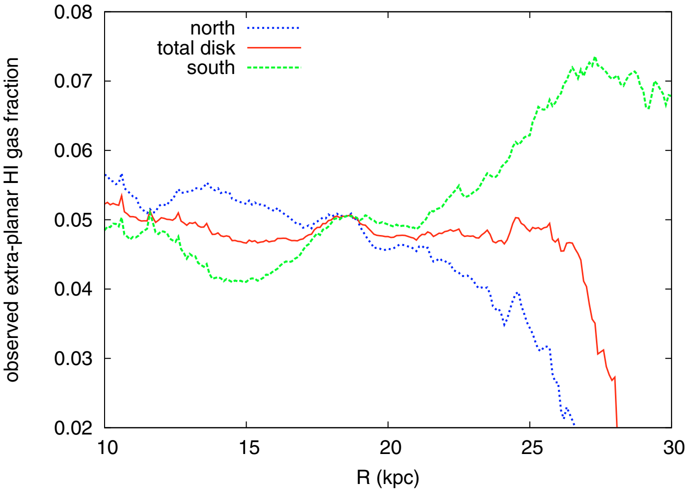

Fig. 12. Fraction of extra-planar gas observed outside the disk for $-15 < z < 20$ kpc.

we calculate the south/north ratios (S/N) for mid-plane volume densities, surface densities and for the scale heights. Figure 11 demonstrates that the asymmetry is strongest for mid-plane volume densities.

We argued in Sect. 4 that the H I gas in the Milky Way behaves on average as expected for an exponential gaseous disk; the surface density is correlated with the product of the mid-plane density and the scale height. This balance, however, does not apply for the asymmetries visible in Fig. 11; there is more gas in the south than in the north. The south/north asymmetry is even more pronounced if we compare the extra-planar gas fraction for $R \gtrsim 25$ kpc (Fig. 12). The northern part of the extra-planar gas appears abruptly torn away to the south for $R \gtrsim 25$ kpc, in the direction of the Magellanic System.

6. Local gas high above the disk

The distribution of planar and extra-planar gas is locally affected by dynamical processes. Here we consider a steady state that is dictated by the necessity of a global balance between gas pressure and gravitational forces. We discuss first how a pressure balance can be achieved by a multi-phase medium, next we use H I line data to verify the derived model. We also compare the extra-planar H I gas in the Milky Way with the anomalous gas phase observed in a few galaxies.

Table 1. Local multi-component gas parameters used for Fig. 13 in comparison to parameters derived from observations (Kalberla et al. 2003).

Component	n_{fit} cm^{-3}	n_{obs} cm^{-3}	σ_{fit} km s^{-1}	σ_{obs} km s^{-1}
hot halo phase	.0018	.0013	60.0	60.0
neutral halo phase	.0014	.0012	74.0	60.0
DIG	.034	.024	26.8	26.8
WNM	0.19	0.10	14.8	14.8
CNM	0.50	0.30	6.1	6.1

6.1. Gravity and vertical gas pressure

For a multi-phase medium, forces acting on the gas due to the pressure gradient $\rho^{-1}\mathrm{d}p/\mathrm{d}z$ need to balance the gravity k_z (e.g. Boulares & Cox 1990) and we may use this property to fit the parameters of the gas distribution. We use the mass distribution provided by Kalberla et al. (2007) to calculate k_z at $R = 8.5$ kpc up to $z = 10$ kpc (Fig. 13). The volume density of the extra-planar gas phase is three orders of magnitude below the density of the other material in the disk. Correspondingly, k_z is unaffected by the halo gas (at the peak, $z \sim 5$ kpc, the influence is $\lesssim 0.3\%$); the extra-planar gas is a genuine tracer of the Galactic potential.

We fit $\rho^{-1}\mathrm{d}p/\mathrm{d}z$ for a multi-component gas to match k_z and obtain agreement with a mean error of 0.6%. In Fig. 13, $\rho^{-1}\mathrm{d}p/\mathrm{d}z$ is over-plotted on k_z; the gas pressure is corrected for a helium abundance of 9% of the hydrogen by number. Essentially, both curves are identical, with differences hardly visible. Table 1 lists the different phases, densities n_{fit} and velocity dispersions σ_{fit} used to balance the gas pressure gradient against the gravitational field. For comparison we give n_{obs} and σ_{obs}, derived previously by fitting the gas distribution in the Solar neighborhood (Kalberla 2003, Table 1). These parameters agree well. The most significant deviation is found for the velocity dispersion of the HVD component. This is a sensitive parameter in fitting the pressure gradient, but is less well determined when fitting observed profile wings. In Sect. 5.2 we used both solutions for comparison.

The shape of k_z for $|z| \lesssim 1.1$ kpc is dominated by the stellar distribution, see Kuijen & Gilmore (1989). We plot their k_z relation for reference. At large z distances we find differences; the dark matter distribution dominates the shape of the k_z function and the gravitational forces become model dependent. The model assumptions by Kuijken & Gilmore (1989) lead to ever-rising forces which are physically implausible. The forces have to decrease at large z distances (Rohlfs 1977). Such a solution was provided by Dehnen & Binney (1998, Galactic Model 2) and we plot their k_z for reference. This model is currently favored for ISM research (Cox 2005 Sect. 2.2) and the downward bending of k_z is interpreted as a shaping provided by the non-planar geometry in the Dehnen & Binney model. In the model of Kalberla (2007) the decrease of the forces at large z distances is caused by the mass associated with the disk. The three k_z curves are discrepant for $k_z \gtrsim 1.1$ kpc. Stars cannot be used to decide between the models but we may use the gas distribution for this purpose.

Attempting to fit the gas phase to match k_z from Dehnen & Binney (1998, Galactic Model 2), we need only 80% of the

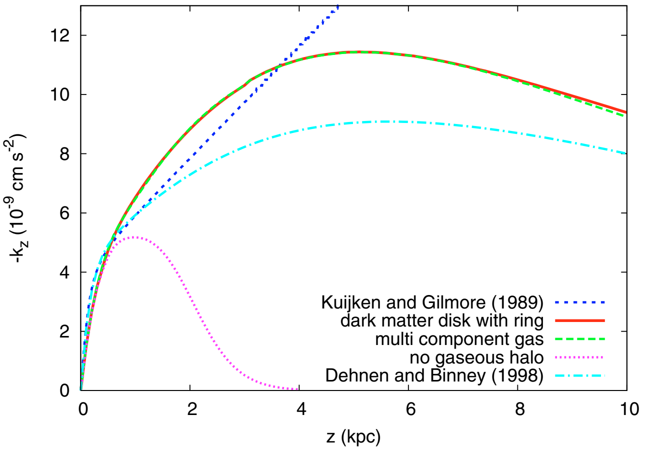

Fig. 13. Gravitational acceleration k_z at $R_\odot = 8.5$ kpc, (solid red line) and gas pressure balance $\rho^{-1}\mathrm{d}p/\mathrm{d}z$ (dotted green). For comparison we plot k_z according to Kuijken & Gilmore (1989) (dashed, blue) and Dehnen & Binney (1998, Galactic Model 2). The lower dotted line gives $\rho^{-1}\mathrm{d}p/\mathrm{d}z$ for a multi-phase gas without halo components.

observed density for the hot halo phase, but 5.5 times the observed density for the neutral halo phase. This, clearly, does not match the observations. We conclude that the observed extra-planar gas phase can be used to constrain dark matter models. Our approach is consistent with the extra-planar gas as observed in the local vicinity. However, some caution is needed. It is not expected that parameters derived at the position of the Sun agree *exactly* with model parameters for $R \sim 8.5$ kpc, since results are dependent on local influences, predominantly caused by the local hot bubble. A hydrostatic model can predict only *global* properties.

Current ISM models (e.g. Cox 2005, Sect. 2.1) do not include a hot or neutral halo phase. For comparison, we plot $\rho^{-1}\mathrm{d}p/\mathrm{d}z$ for the fitted parameters from Table 1, but without a hot or neutral halo phase. This makes a huge difference. For a global pressure balance at large z distances a halo gas phase is unambiguously needed. Preliminary evidence for such a phase from interstellar absorption lines was given by Münch & Zirin (1961). Lockman & Gehman (1991) have shown that more than two H I components are needed to explain the average local H I emission. In the next section we discuss the observational evidence for a multiphase H I component in more detail. We show H I emission resulting from a neutral halo gas phase and demonstrate how the observations compare with the model given in Table 1.

6.2. The polar caps in H I

Figure 14 displays the average H I emission measured at the north polar cap for $b > 20°$. We use $\log(T_\mathrm{B})$ to compress the huge dynamic range of the H I emission. We compare data from the Bell labs survey (Stark 1992, Fig. 10) with data from the LAB survey (Kalberla et al. 2005). Both agree well, except for the wings at high velocities. Observational shortcomings cause the discrepancy. The bandwidth of the Bell labs filter bank was too small to cover the necessary velocity range completely; it needed to be shifted in velocity to obtain the main H I emission. The outer two channels of the filter bank were defined to be zero for all spectra. The weights (in dB, dashed line) show how this affects the mean Bell labs emission spectrum. As the weights decrease, the average Bell labs profile becomes incomplete and biased.

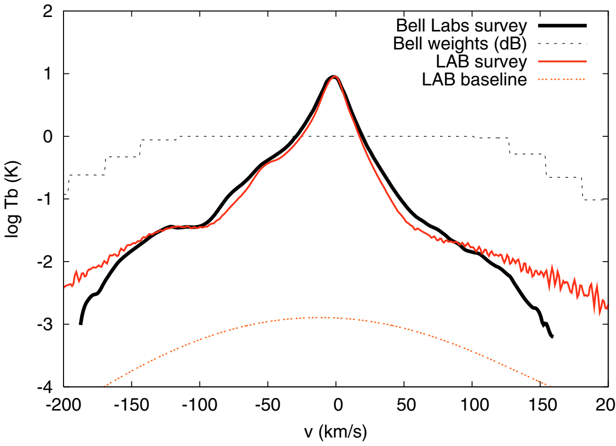

Fig. 14. Average H I emission to logarithmic scale for latitudes $b > 20°$. The data are from the Bell Labs telescope (thick black line) and from the LAB survey (red). The step function shows the weights for each channel in dB. The thin red dotted line represents broad Gaussian components indicating baseline problems.

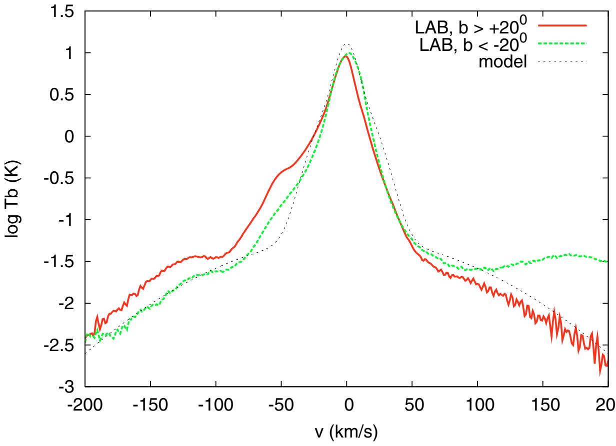

Fig. 15. Average H I emission in logarithmic scale for latitudes $|b| > 20°$ from the LAB survey. The red line is for the north polar cap, the dashed green line for the southern part. The thin dotted black line represents the model according to Table 1.

The LAB survey may be influenced by systematic errors, too. The lower red dotted curve in Fig. 14 shows the mean of all broad LAB Gaussians, most probably representing baseline defects in the LAB survey (Haud & Kalberla 2006). This is two orders of magnitude below the mean emission; the weak profile wings are significant.

Figure 15 compares the LAB data for the northern and southern polar caps. We also plot the model distribution according to our best fit mass model, using the fitted parameters for the H I components from Table 1. Note that the fit was to match $\rho^{-1}\mathrm{d}p/\mathrm{d}z$ with k_z, but no fit was applied to the plotted profile in Fig. 15, and to the wings in Figs. 8 and 9. All profiles in Fig. 15 show extended wings, but with some systematic differences. The enhanced emission for $v_\mathrm{lsr} \gtrsim 100$ km s^{-1} at the southern polar cap is due to the Magellanic Stream. We find enhancements at $v_\mathrm{lsr} \sim -60$ km s^{-1}, caused by distinct IVCs and at $v_\mathrm{lsr} \sim -120$ km s^{-1}, caused by HVCs.

The broad wing underlying the CNM and WNM emission in Fig. 15 is caused by extra-planar gas, the HVD component.

Numerous clumps, filaments, and spurs, located above the CNM and WNM disk, contribute to a signal which can be well represented by a weak component with a large velocity dispersion. We conclude that the *local* observed extra-planar H I gas distribution, forced to be on average in pressure balance $k_z \sim \rho^{-1} \mathrm{d}p/\mathrm{d}z$ (Fig. 13), is consistent with the gas component that was proposed in Sect. 5.2 to explain the gas distribution at the *outskirts* of the Galaxy. Systematic differences are caused by a warped and asymmetric gas distribution. Gas in the southern part of the outer Milky Way appears to be enhanced. This is consistent with the enhanced positive velocity wing in Fig. 15 for $b < 20°$. The negative profile wing is enhanced for $b > 20°$ due to the warp that bends up to the north.

6.3. Extra-planar gas fraction

During our analysis we distinguished disk emission and extra-planar gas. For a safe determination of the first moments of the stationary disk gas we masked and excluded outliers of the H I volume density distribution which are most probably not associated with the disk. This part of the $n(R, Z, \phi)$ distribution has radial velocities that are incompatible with a circular rotation of the disk gas around the Galactic center. Individual features show up as sheets and filaments in the $n(R, Z, \phi)$ distribution (see Fig. 1 or Kalberla et al. 2007, Sects. 2.2 and 3). The corresponding clouds, visible in the $T_\mathrm{B}(l, b, v)$ distribution (Fig. 10), are usually classified as HVCs and IVCs. In general it is assumed that IVCs are located in the lower Galactic halo while HVCs are at larger distances (Albert & Danly 2004).

For a determination of the extra-planar gas fraction we use a range where the properties of the Galactic disk are well defined, $10 \lesssim R \lesssim 30$ kpc. On average we find there direct evidence that about 5% of the H I is not associated with the disk (Fig. 12). This estimate is independent of the mass model used. Using parameters from Table 1, integrating for $R \lesssim 50$ kpc, we derive that the HVD component amounts in total to 10% of the gas. This discrepancy is explained by the fact that most of the HVD gas phase in the Milky Way cannot be distinguished from the CNM/WNM gas phase. Only gas at the wings of the HVD distribution is counted and we estimate that about 50% of this gas remains undetected by our filter and revise the extra-planar gas fraction to be 10%, consistent with the HVD model.

6.4. Anomalous gas in the Milky Way, an external viewpoint

To compare the Milky Way with sensitive observations of other galaxies, we take the viewpoint of an external observer. The H I emission is synthesized accordingly. We use a flat disk without warp at an inclination of 80° and calculate the total emission along the line of sight. The contours in Fig. 16 represent observable column densities, normalized and plotted in steps of 2 dB. We consider observations with a limited dynamic range of 30 dB; the lowest contour is at –30 dB.

The simulated position velocity diagram shows that the velocity at the peak of the line emission is identical with the rotation curve from the model. The average observable rotation velocity for the halo gas phase alone, determined from the peak emission of the halo gas phase lags behind. The total column density distribution is symmetric at large column densities, but as a consequence of the lagging halo some asymmetries appear at low levels. Projection effects cause extended regions with H I emission at lower velocities. Such features at levels below –20 dB were first observed in NGC 891 (Swaters et al. 1997), the so-called beards (Fraternali et al. 2001). Close to the center, the beards extend to forbidden velocities, mimicking an apparent counter-rotation.

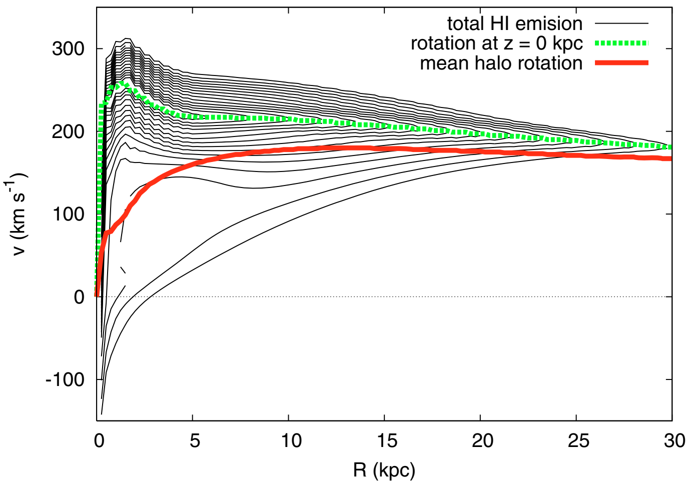

Fig. 16. Position velocity diagram along the major axis, observable for a galaxy like the Milky Way with an inclination of 80°. The thin contours represent normalized column densities in steps of 2 dB; the lowest contour is at –30 dB. The green dashed lines gives the rotation curve at $z = 0$ kpc, the solid red line the mean rotation for the H I in the halo.

Beards and forbidden velocities in Fig. 16 have the same origin. The line of sight passes through various layers of extra-planar gas that rotate slower than the disk. The lag is approximately constant for $z/h_z(R)$ with z distances normalized to scale heights (Kalberla 2003, Fig. 11). For small radii, the densest part of the thick extra-planar gas disk close to the center becomes most prominent. The lag is most pronounced there.

Our model takes both the flaring and lagging halo into account. Both are necessary to explain the observations. The beards in Fig. 16 originate from the same H I halo gas phase that causes the extended wings in Figs. 14 and 15. At the end of this subsection we point out that an external observer, with a telescope that is limited in dynamic range to 30 dB, would see the Galactic H I disk out to $R \sim 30$ kpc only. At low levels it is far easier to find extended emission perpendicular to the disk as shown recently by Oosterloo et al. (2007) in the case of NGC 891. Reaching the outskirts at distances of $R \sim 50$ kpc, is a demanding task and needs a dynamic range of 40 dB or better. The HVD component at such radii is essentially invisible.

7. Summary and discussion

We used the LAB survey to derive the H I volume density distribution in the Milky Way. The $T_\mathrm{B}(l, b, v)$ to $n(R, z, \phi)$ conversion depends on the rotation curve; we have chosen an almost flat curve with lagging rotation for gas above the mid-plane (Kalberla et al. 2007). The corresponding mass model implies that some of the dark matter is associated with a thick exponential disk.

Our aim was to derive global properties for the H I gas distribution in the Milky Way. We calculated the first moments to determine surface densities, mid-plane positions, associated mid-plane densities, and scale-heights. Planar and extra-planar gas was distinguished by applying adaptive filters. We discuss mid-plane positions first.

7.1. The warp

The Galactic warp can be traced from $R \sim 12.5$ kpc out to $R \sim 45$ kpc but the coherent structure is lost for $R \gtrsim 40$ kpc. The scalloping power, defined by the squares of the amplitudes from a sine wave fit, is below 0.6% in the inner part of the disk. For $30 \lesssim R \lesssim 45$ kpc we observe a linear increase up to 3% of the total warp power.

7.2. The exponential H I disk

We derive average surface densities and, taking the warp into account, average volume densities at mid-plane. In both cases we find significant fluctuations and asymmetries between north and south which are correlated. Surface densities and mid-plane volume densities are affected by spiral structure, but differences between north and south need to be explained by an asymmetric disk (Levine et al. 2006a,b; Kalberla 2007).

Average surface densities, mid-plane volume densities, and scale heights can be approximated over a broad radial range by exponential relations. For the surface density we find a scale length of 3.75 kpc within $12.5 \lesssim R \lesssim 30$ kpc. Mid-plane volume densities are well approximated with a scale length of 3.15 kpc for $7 \lesssim R \lesssim 35$ kpc. Both relations imply that the scale heights also can be described well by an exponential relation, in this case valid for $5 \lesssim R \lesssim 35$ kpc.

For $R \lesssim 12.5$ kpc we find approximately constant surface densities ($\Sigma_{\rm inner} \sim 10\ M_\odot\ {\rm pc}^{-2}$). This is also the inner part of the H I disk which is unaffected by the warp.

7.3. The Galactic outskirts

The exponential disk approximation for the disk gas breaks down in all respects at radial distances $R \gtrsim 35$ kpc. In the outer part we find a shallower distribution which can be approximated by a gas phase with a radial scale length of 7.5 kpc and a high velocity dispersion of 74 km s^{-1}.

Our results are apparently in disagreement with Maloney (1993), who found a sharp truncation of the neutral hydrogen distribution for the outer disk H I gas in NGC 3198 at a surface density level $10^{18} \lesssim N_{\rm H} \lesssim 10^{19}$ cm^{-2}. This limit is attributed to the extragalactic radiation field. To study the origin of the HVD component at large distances we examined the data. At a distance of 60 kpc the telescope beam covers a typical area of 600 pc in diameter. Any emission within this area is smoothed out completely. Inspecting the data cube visually, we find regions with peak densities of $n(R) \sim 10^{-3}$ cm^{-3}, surrounded by less dense envelopes. These unresolved individual condensations may be well above the predicted cut-off limit.

Maloney's interpretation was questioned recently by Oosterloo et al. (2007) who found that a deeper mapping of NGC891 led predominantly to the detection of unknown low level emission in the vertical direction, while the radial limits remained. Such an asymmetry is unexpected for an isotropic radiation field. Our analysis shows the same trend. At the outskirts of the disk the HVD component becomes most extended in z direction. Mid plane volume densities are dominated by the HVD component for $R \gtrsim 40$ kpc, while surface densities (integrated in z direction) show the same effect for $R \gtrsim 35$ kpc (compare Figs. 8 and 9).

7.4. Polar caps and extra-planar gas

The H I gas distribution, averaged over all latitudes $|b| > 20°$, probing approximately the local volume within a radius of 1 kpc, has broad profile wings. These wings may be affected by stray radiation of the telescope, but for the Bell Labs and the LAB survey they are not explainable by instrumental problems. The same HVD component with a dispersion of 74 km s^{-1}, which was used to fit the gas distribution in the outskirts, is useful also to explain this local component. A multi-phase medium containing this HVD component is found to balance gravity by its pressure gradient, $k_z \sim \rho^{-1} {\rm d}p/{\rm d}z$ for the mass model proposed by Kalberla et al. (2007).

7.5. Clumps, fast and at large z distances

Evidence for a population of fast gas clouds with a velocity dispersion of $\sigma \sim 35$ km s^{-1}was found by Radhakrishnan & Srinivasan (1980); Kulkarni & Fich (1985); Lockman & Gehman (1991); Mohan et al. (2004). Kalberla et al. (1998), analyzing the Leiden/Dwingeloo Survey, proposed a more extreme dispersion of $\sigma \sim 60$ km s^{-1}which is modified here to $\sigma \sim 74$ km s^{-1}. Most remarkable, however, is the early prediction by Pikelner & Shklovsky (1958) who proposed a neutral halo gas phase with $\sigma \sim 70$ km s^{-1}.

The HVD component analyzed here as a diffuse emission component with a dispersion of $\sigma \sim 74$ km s^{-1}, is patchy. It is made up of a large number of filaments and small H I clumps. These stand out from the normal disk emission only if they reach large z distances or if they have high forbidden velocities. Evidence for such clumps in the inner Galaxy was given by Lockman (2002b). Stanimirović (2006) found similar clumps in the anti-center direction. Clouds with high forbidden velocities in the inner Galaxy were detected by Stil et al. (2006) in the VLA Galactic Plane Survey. These authors estimate that this population of fast clouds has a radial scale length of 2.8 to 8 kpc, consistent with the scale length of 7.5 kpc derived by us.

7.6. Extra-planar gas fraction

For our analysis we used adaptive filters to distinguish the stationary disk component from extra-planar gas. Over the main body of the disk ($10 \lesssim R \lesssim 30$ kpc) we measure that on average 5% of the gas is outside the disk (Fig. 12). This is a lower limit only. Assuming that the extra-planar gas can be characterized as an HVD component implies that a significant fraction of this phase is hidden from direct observation since it cannot be distinguished from disk gas. For our analysis we estimate that only 50% of the LVD gas can be discriminated, resulting in an extra-planar gas fraction of 10%. This is consistent with a hydrostatic model (Sect. 6.1), observations at the polar caps (Sect. 6.2) and also with the gas distribution at the Galactic outskirts (Sect. 5.2). We conclude that *all over the Galactic* H I *disk* the "normal" phase, the CNM and WNM, is associated by an "anomalous" gas phase, described here as an HVD phase. For the inner Galaxy ($R \lesssim 10$ kpc) we observe an increase of the extra-planar gas fraction of a few percent. This might be explained by fountain activities but, as discussed in Sect. 2, estimates at such distances are highly uncertain.

In this light, the general features of the extra-planar H I gas in NGC 891 and NGC 2403 appear to be comparable (within a factor of 2) to what we see in the Milky Way. This is confirmed by projecting the H I gas distribution of the Milky Way to large distances. Simulating position-velocity diagrams, the HVD component causes wings and beards close to the center. The gaseous outskirts, however, would hardly be observable. The telescope sensitivity needs to be improved by a factor of 10 to observe this part, which is feasible with the SKA.

7.7. HVC and IVC gas

HVCs and IVCs are usually classified from observations according to their velocities. One can distinguish between coherent complexes and isolated compact objects. Their origin may be from fountain flow or accretion. Also, metalicities are important but here we discuss H I properties only.

For our analysis of the global properties of the H I distribution we have chosen different criteria. The primary goal was to derive the properties of the main body, the H I disk. This has a well defined dynamically cool gas distribution. There are two phases, CNM and WNM, both with velocity dispersions perpendicular to the disk that are low compared to the rotation velocity. The gas disk is flaring but the most prominent inner part of the H I disk is highly flattened.

However, as proposed by Spitzer (1956) and much later established by X-ray observations of the predominantly hot ISM of elliptical galaxies, the hot Galactic ISM does not have to be so flat. The extra-planar H I is embedded in the hot component. This arises the question of whether there might be a quasi-static system near equilibrium as modeled by Spitzer or whether the Milky Way halo is strongly affected by steadily changing conditions, e.g. due to mass inflow or star bursts.

The star-formation-rate (SFR) in the solar neighborhood is remarkably constant over the lifetime of the disk, infall of material appears also to be approximately constant at one-half of the SFR (Twarog 1980). Ongoing accretion may be derived from HVC complexes and also from the Magellanic Stream but it is unclear whether irregularities in accretion rate and outflows are strong enough to affect the global shape of the Galactic halo significantly. Little is known about the impact of star bursts on the structure and dynamics of the Milky Way halo. Supershells and chimneys may reach z distances of several kpc but appear not to be able to shape a significant fraction of the halo (McClure-Griffiths et al. 2006).

As a halo model therefore we have chosen the simple case of a quasi-static system that can be approximated numerically by a hydrostatic distribution. We are interested in *global* properties of the gas distribution, not in details that are more important for individual components. A global model makes sense when averaging the H I emission over several kpc as we obtain a self-consistent solution. As discussed in Sects. 5 and 6, the same model parameters apply to both polar caps and to the sectors $50° \lesssim \phi \lesssim 130°$ and $250° \lesssim \phi \lesssim 310°$ at $40 \gtrsim R \gtrsim 60$ kpc. These are the only regions available for an unambiguous separation of planar and extra-planar gas in the Milky Way.

Figure 10, a l–v plot of measured brightness temperatures, displays numerous IVCs and HVCs. These features appear partly to be organized in complexes but are in general close to the disk. Projection effects cause a complicated picture, in particular velocity crowding in some parts of the sky makes it difficult to judge whether a particular feature belongs to the disk or not. Deviation velocities between planar and extra-planar gas components depend strongly on position.

The density distribution $n(R, z, \phi)$ in Fig. 1 shows a clearer picture. Extra-planar gas is offset from the Galactic disk but most of it is clearly associated with the disk. Again we find large scale fluctuations but there is a general trend that the extra-planar gas distribution increases with decreasing mid-plane distance. This situation appears best to be described as a "thick disk" having twice the radial scale length of the CNM/WNM gas distribution. We use the model of a turbulent HVD distribution. Local enhancements, or complexes, are considered as statistical fluctuations; they become less dominant if one averages over larger areas, this is a typical property of a turbulent medium. Figure 15, showing average emission of the polar caps at latitudes $|b| > 20°$ also includes IVCs, HVCs, and the Magellanic stream. These local phenomena show up as minor perturbations.

Comparing properties of the HVD component with global properties of the HVC gas we find some interesting agreements. HVCs have a multi-phase structure and are most probably confined by an external hot halo phase (Kalberla & Haud 2006). HVCs have specific turbulent energy densities that are an order of magnitude higher than that of comparable clumps in the Galactic disk. The same conditions hold for the HVD component. Most surprising, however, is that the integrated flux distribution for HVCs as function of velocity Wakker (1991, Fig. 5) is a continuation of the gas distribution in the broad wings of the HVD component to high velocities (Fig. 15).

The HVD component is coupled to the disk but it is anomalous in the sense that it represents a highly turbulent clumpy phase, best described as an extended very thick disk. At the position of the Sun we determine an exponential scale height of 3.9 kpc. The HVD component can be best characterized as an extra-planar gas component; it expands the phase space occupied by the H I disk predominantly perpendicular to the disk. IVCs are located in the lower Galactic halo (Albert & Danly 2004). Their velocities as well as known z distances place them at the less distant part of the HVD phase space. Distances for HVCs are less well known but according to their velocities at least some of them may belong to the outer part of the HVD phase space. The HVC velocity limit is $|v_{\rm lsr}| = 465$ km s^{-1}, roughly coincident with the escape velocity of the Milky Way.

Individual extra-planar gas layers are extremely patchy and lag behind the underlying rotating disk. These layers are affected by flaring and the lag depends on the distance $z/h_z(R)$, normalized to the disk scale height. The anomalous gas phase is rather extended. We could trace it up to $R \sim 60$ kpc.

The gravitational potential at the outskirts of the Milky Way is very shallow. The rotation of anomalous gas for $R \gtrsim 35$ kpc is therefore essentially unaffected by flaring. The fact that we observe an extended HVD gas phase at $40 \lesssim R \lesssim 60$ kpc implies accretion by a "drizzle" of low mass fragments. This gas cannot originate from fountain flows. Fountain events far outside R_{25} are highly improbable as the radial scale lengths for stars and HVD gas differ significantly.

A continuous flow of material in galaxies from the disk into the halo was studied by Collins et al. (2002); Fraternali & Binney (2006; Heald et al. (2006a). Their models can explain the vertical gas distribution but fail to reproduce the apparent counter rotation and vertical velocity gradients. They also produce a general outflow, contrary to observations.

7.8. The lopsided H I distribution

Our aim was to describe global features of the H I distribution that may be representative of a steady state. Calculating radial distribution functions we found in all cases significant systematic differences between the northern and southern part of the Milky Way. The system is asymmetrical. Midplane volume densities and surface densities are most discrepant at $R \sim 20$ kpc. Considering the H I flaring we found a systematic modulation that may be explainable by a misaligned gravitational field originating from a misaligned dark matter disk (Fig. 11). The flaring ratio peaks at $R \sim 25$ kpc are in excellent agreement with Weinberg (1998) who predicted that the interaction between Milky Way and Magellanic system causes a dark matter wake at this position.

7.9. Rotation curve and mass distribution

Our results depend on the rotation curve, hence on the mass model. We tested several different possibilities and summarize briefly how much our conclusions are affected by the mass model used (Kalberla et al. 2007).

The global surface density distribution, mid plane densities and also flaring depend weakly on the rotation curve (Voskes 1999; Nakanishi & Sofue 2003; Levine et al. 2006a,b) but our results are not altered significantly as long as a nearly flat rotation curve is used. The radial exponential scale length of 3.75 kpc derived by us changes to 4 kpc if one uses a constant rotation with a circular velocity of 220 km s^{-1}. Our conclusion that surface densities, mid plane densities and flaring can be approximated by exponential relations remains valid, although the correlation degrades somewhat if we use alternative rotation curves.

Deviations from axisymmetry depend on non-circular terms in the rotation curve. We used the first order epicyclic streamline correction by Levine et al. (2006a, Eqs. (1), (2)) which is a great improvement in overcoming discontinuities at large radial distances. This correction is empirical but the assumption that surface densities should not have azimuthal discontinuities remains valid for all mass models. The correction is consistent with an asymmetrical mass distribution and the results do not depend significantly on the details of the mass model. The same holds for asymmetries in the H I distribution.

The average H I emission at the polar caps (Sect. 6.2) has broad high velocity wings. This is known from observations. Parameters for the underlying HVD component are completely independent of any mass model. The parameter fitting, assuming halo gas in global hydrostatic equilibrium with the gravitational field, depends strongly on the mass model. A dependence on the mass model exists also for HVD gas at the outskirts of the Milky Way. It is the shape of the outer rotation curve that determines the distance of this component.

We argued that the thin H I disk, defined by the CNM & WNM gas, is associated with a thick extended HVD gas disk. This model is self-consistent for the mass model used but it necessarily has to break down for significant changes of the mass model or the outer rotation curve.

Acknowledgements. This project was supported by Deutsche Forschungsgemeinschaft, grant KA1265/5-1. We thank J. Kerp and F. Kenn for discussions and a careful reading of the manuscript and the anonymous referee for constructive criticism.

References

Albert, C. E., & Danly, L. 2004, ASSL: High Velocity Clouds, 312, 73
Bajaja, E., Arnal, E. M., Larrarte, J. J., et al. 2005, A&A, 440, 767
Binney, J., & Merrifield, M. 1998 (Princeton, NJ: Princeton University Press)
Boulares, A., & Cox, D. P. 1990, ApJ, 365, 544
Collins, J. A., Benjamin, R. A., & Rand, R. J. 2002, BAAS, 34, 709
Cox, D. P. 2005, ARA&A, 43, 337
Dame, T. M. 1993, Back to the Galaxy, 278, 267
de Avillez, M. A. 2000, MNRAS, 315, 479
de Boer, W., Sander, C., Zhukov, V., Gladyshev, A. V., & Kazakov, D. I. 2005, A&A, 444, 51
Dehnen, W., & Binney, J. 1998, MNRAS, 294, 429
Dickey, J. M., & Lockman, F. J. 1990, ARA&A, 28, 215
Diplas, A., & Savage, B. D. 1991, ApJ, 377, 126
Fraternali, F., & Binney, J. J. 2006, MNRAS, 366, 449
Fraternali, F., Oosterloo, T., Sancisi, R., & van Moorsel, G. 2001, ApJ, 562, L47
Fraternali, F., Oosterloo, T., Boomsma, R., Swaters, R., & Sancisi, R. 2004, IAU Symp., 217, 136
Hartmann, D., & Burton, W. B. 1997, Atlas of Galactic Neutral Hydrogen (Cambridge: Cambridge University Press)
Haud, U., & Kalberla, P. M. W. 2006, Baltic Astron., 15, 413
Heald, G. H., Rand, R. J., Benjamin, R. A., Collins, J. A., & Bland-Hawthorn, J. 2006, ApJ, 636, 181
Henderson, A. P., Jackson, P. D., & Kerr, F. J. 1982, ApJ, 263, 116
Kalberla, P. M. W. 2003, ApJ, 588, 805
Kalberla, P. M. W., & Haud, U. 2006, A&A, 455, 481
Kalberla, P. M. W., Westphalen, G., Mebold, U., Hartmann, D., & Burton, W. B. 1998, A&A, 332, L61
Kalberla, P. M. W., Burton, W. B., Hartmann, D., et al. 2005, A&A, 440, 775
Kalberla, P. M. W., Dedes, L., Kerp, J., & Haud, U. 2007, A&A, 469, 511
Kuijken, K., & Gilmore, G. 1989b, MNRAS, 239, 651
Kulkarni, S. R., & Fich, M. 1985, ApJ, 289, 792
Kulkarni, S. R., Heiles, C., & Blitz, L. 1982, ApJ, 259, L63
Levine, E. S., Blitz, L., & Heiles, C. 2006a, ApJ, 643, 881
Levine, E. S., Blitz, L., & Heiles, C. 2006b, Science, 312, 1773
Lockman, F. J. 1988, The Outer Galaxy, 306, 79
Lockman, F. J. 2002a, Seeing Through the Dust: The Detection of HI and the Exploration of the ISM in Galaxies, 276, 107
Lockman, F. J. 2002b, ApJ, 580, L47
Lockman, F. J. 2004, Recycling Intergalactic and Interstellar Matter, 217, 130
Lockman, F. J., & Gehman, C. S. 1991, ApJ, 382, 182
McClure-Griffiths, N. M., Ford, A., Pisano, D. J., et al. 2006, ApJ, 638, 196
Maloney, P. 1993, ApJ, 414, 41
Mohan, R., Dwarakanath, K. S., & Srinivasan, G. 2004, J.A&A, 25, 185
Münch, G., & Zirin, H. 1961, ApJ, 133, 11
Nakanishi, H., & Sofue, Y. 2003, PASJ, 55, 191
Oosterloo, T., Fraternali, F., & Sancisi, R. 2007, AJ, 134, 1019
Lockman, F. J., & Shields, J. C. 2007, ApJ, 656, 928
Pikelner, S. B., & Shklovsky, I. S. 1958, Rev. Mod. Phys., IAU Symp. 8, 30, 935
Radhakrishnan, V., & Srinivasan, G. 1980, A&A, 1, 47
Rohlfs, K. 1977, Lect. Notes Phys. (Berlin: Springer Verlag), 69,
Saha, K., & Jog, C. J. 2006, MNRAS, 367, 1297
Spitzer, L. 1942, ApJ, 95, 329
Spitzer, L. J. 1956, ApJ, 124, 20
Stanimirović, S., Putman, M., Heiles, C. P., Joshua, E. G., & Goldsmith, P. F. 2006, ApJ, 653, 1210
Stark, A. A., Gammie, C. F., Wilson, R. W., et al. 1992, ApJS, 79, 77
Stil, J. M., Lockman, F. J., Taylor, A. R., et al. 2006, ApJ, 637, 366
Swaters, R. A., Sancisi, R., & van der Hulst, J. M. 1997, ApJ, 491, 140
Twarog, B. A. 1980, ApJ, 242, 242
van Woerden, H., Wakker, B. P., Schwarz, U. J., & de Boer, K. S. 2004a, High Velocity Clouds, ASSL, 312
Voskes, T. 1999, M.Sc. Thesis, University of Leiden, `[arXiv:astro-ph/0601653]`
Wakker, B. P. 1991, A&A, 250, 499
Weinberg, M. D. 1998, MNRAS, 299, 499
Weiner, B. J., & Sellwood, J. A. 1999, ApJ, 524, 112
Wolfire, M. G., McKee, C. F., Hollenbach, D., & Tielens, A. G. G. M. 2003, ApJ, 587, 278
Wouterloot, J. G. A., Brand, J., Burton, W. B., & Kwee, K. K. 1990, A&A, 230, 21